nature materials

SUPPLEMENTARY INFORMATION

DOI: 10.1038/NMAT3638

Proton trapping in yttrium-doped barium zirconate

Yoshihiro Yamazaki[1,2]*, Frédéric Blanc[3], Yuji Okuyama[2], Lucienne Buannic[4], Juan C. Lucio-Vega[2], Clare P. Grey[3,4], and Sossina M. Haile[2]

1 Japan Science and Technology Agency, PRESTO, 4-1-8 Honcho, Kawaguchi, Saitama, 332-0012, Japan

2 Materials Science Department, California Institute of Technology, 1200 E. California Blvd., Pasadena, CA 91125, USA

3 Department of Chemistry, University of Cambridge, Lensfield Rd, Cambridge, CB2 1EW, UK

4 Department of Chemistry, Stony Brook University, Stony Brook, NY 11794-3400 USA

* corresponding author: yamazaki@caltech.edu

DOI: 10.1038/NMAT3638

Materials and Methods

Sample Preparation

Powders of $Ba_{0.97}Zr_{0.79}Y_{0.21}O_{3-\delta}$ (BYZ20) were synthesized using a chemical solution method[1]. Compacts (19 mm in diameter and 3~4 mm in thickness) were prepared by isostatic pressing, and these were then sintered at 1580 °C for 24 h under flowing air to obtain samples of greater than 92% of theoretical density. For NMR measurements, sintered pellets were lightly crushed to obtain 45-75 mm sized particles. For AC impedance, conductivity exchange, and electron probe microanalysis measurements (the latter used for determining chemical composition), dense pellets were cut and polished to attain mirror-like surfaces and a thickness of 0.45 and 0.77 mm. For electrical measurements 1 μm silver film was deposited on both surfaces of the pellet by DC sputtering. Each sample was then sandwiched between silver mesh current collectors and annealed at 700 °C for 2 hr under air, creating a structure with interconnected porous silver electrodes firmly adhered to the silver current collectors. (Figure S1). TGA measurements were performed on samples corresponding to both the conductivity and NMR sample types. Specifically, for the former, dense compacts with porous silver electrode layers (but excluding the mesh current collector) were employed. For latter, coarse powders obtained by lightly grinding sintered compacts were utilized.

Electron probe microanalysis was carried out using a JEOL 8200 and $BaTiO_3$, $ZrSiO_4$ and YPO_4 standards.

Thermogravimetric analysis

Thermogravimetry was performed using a Netzsch simultaneous thermal analyzer, Jupiter 449C. Experiments were carried out to obtain water uptake behavior corresponding to both the ACIS conductivity and the NMR experiments. To reflect the ACIS experiments, 0.72 g of BYZ20 pellets (with porous silver electrode layers) were heated to 800 °C and held there for an hour under dry, high-purity nitrogen pre-mixed with 10 ppm oxygen. This step removes possible hydroxides, carbonates, and surface water and establishes a reference state. The gas was then saturated with water (pH_2O = 0.023 atm), and the weight increase was recorded at several temperatures upon cooling from 800 to 34 °C at a rate of 10 °C/min. The equilibration time at 710 and 610

°C was 1 hr and 15 min at lower temperatures. To mimic the NMR experiments, coarse powders, ~ 2 g per measurement, were treated in a similar manner. The initial dehydration step was carried out at 1000 °C, the cooling rate was 10 °C/min, data were recorded at 50-100 C increments, and the equilibration time at each temperature was 30 min down to 412 °C and 2 hr at 360 °C and below. Both types of measurements were repeated multiple times to ensure reproducibility (six times for compacts and four times for powders).

The low specific surface areas of the samples avoid complications due to surface hydration observed for high surface area materials. With this simplification and the assumption that the entirety of the weight gain under humid conditions is due to hydration of the perovskite (valid at temperatures below which oxidation by H_2O may occur[2]), the TGA results directly yield the proton content. Furthermore, the small surface to volume ratio quenches the (de)hydration kinetics on the time scale of interest at temperatures ≤ 300-400 °C, Figure S3, and the bulk proton concentration can be considered fixed.

Electrical Measurements

AC impedance data for both conductivity and diffusivity (exchange) measurements were collected using a Solartron 1260 in the frequency range 0.1 Hz to 13 MHz (a voltage amplitude of 30 mV). Using a thermal protocol almost identical to that employed for TGA measurements, the BYZ20 pellet was heated to 715 °C under dry, high-purity nitrogen pre-mixed with 10 ppm oxygen, and held there for an hour to dehydrate and remove possible surface carbonates. The gas was then saturated with water ($pH_2O = 0.023$ atm measured using a HygroFlex hygrometer, Rotonix Inc.) and held under such conditions for an hour to achieve hydration. The conductivity was measured upon cooling from 715 to 34 °C at 10 °C/min and recorded at several temperatures with an equilibration time of 1 h at 615 °C and 15 min at lower temperatures. The bulk conductivity was differentiated from the grain boundary conductivity at 363 °C and below. The measurements were repeated four times to check the reproducibility. The impedance spectra displayed well-resolved arcs in the Nyquist representation, Figure S2, and were analyzed in terms of an equivalent circuit model in which (depending on the

DOI: 10.1038/NMAT3638

temperature regime) distinct RQ subcircuits were used to represent the grain interior, grain boundary, and electrode regions. Here, R is an ideal resistor with $Z_R = R$ and Q is a constant phase element with $Z_Q = (Y(j\omega)^n)^{-1}$, where j is $\sqrt{-1}$, ω is the frequency, and Y and n are constants with $0 < n < 1$.

H_2O-D_2O exchange experiments were carried out at 628~715 °C. In this temperature range the proton conductivity is approximately 40% greater than that of the deuterium ion conductivity and, upon a change in atmosphere from one that is saturated with D_2O to one that is saturated with H_2O, the conductivity increase is easily detected, Figure S5. The impact of grain boundaries on the conductivity is negligible in this temperature range. The rate of change reflects the ambipolar diffusion coefficient[3], $\tilde{D}_{HD}$,without contribution from the electronic holes and oxygen vacancies, as these have fixed concentrations during the exchange process. The BYZ20 pellet was first heated to 715 °C under dry, high-purity nitrogen pre-mixed with 10 ppm oxygen. After 1 hr the gas was switched to heavy water (pD_2O = 0.028 atm, D_2O, Cambridge Isotope Laboratories, Inc. 99.9%) and the sample allowed to equilibrate, typically requiring > 12 hr, as determined by an unchanging impedance response. From the full Nyquist representation (0.1 Hz to 13 MHz), an example of which is presented Figure S2 (c), a measurement frequency yielding an entirely real impedance value that also corresponded to the bulk response was selected for subsequent single-frequency measurements. The flowing gas was then abruptly changed from D_2O- to H_2O-saturated nitrogen (pH_2O = 0.027 atm) and the change in conductivity recorded by collecting data every 17 s in the single-frequency mode. The water partial pressure was monitored using a HygroFlex hygrometer, whereas the heavy water partial pressure was calculated from the water bath temperature[4]. Almost complete recovery in resistance after returning to a D_2O atmosphere was also confirmed. The numerical value of $\tilde{D}_{H-D}$ was determined at each measurement temperature using the non-steady state solution to Fick's second law for one-dimensional diffusion into a plate (see Supplemental Figure S5).

NMR Measurements

High Temperature ^{1}H MAS NMR experiments were performed on a 8.45 T Varian Oxford Infinity Plus 360 MHz spectrometer equipped with a 7 mm HX high temperature

MAS probe from Doty Scientific, Inc. Prior to NMR data collection, coarse powder samples were hydrated in a manner almost identical to that employed for hydration of the reference powder samples. Specifically, powder was heat-treated at 1000 °C for an hour under flowing dry high-purity N_2 to remove possible hydroxides and hydrocarbons formed on the surface. The atmosphere was then saturated with water vapor (pH_2O = 0.028 atm) by passing it through a room temperature bubbler and the sample cooled in 100 °C increments at a rate of 10 °C/min with 2 hr equilibrations at each temperature. Upon reaching 350 °C, hydrated samples were quickly removed from the furnace to quench the hydration state and transferred to a glove box to minimize hydroxide formation on the powder surface. There they were packed in boron nitride (BN) inserts, and placed in 7 mm silicon nitride (Si_3N_4). NMR experiments were carried out at a MAS frequency of 4 kHz at room temperature and 50 °C and at 6 kHz at 100 °C and above using a radio-frequency field amplitude of 50 kHz. Recycle delays of 0.5 s yielding quantitative spectra were used (see Figure S11). Spin lattice relaxation times T_1 were determined by inversion recovery experiments and subsequent spectral deconvolution, and the signal intensity fitted to $I = I_0\left[1 - a\exp(-\tau / T_1)\right]$ (where I_0 is the initial signal intensity, a is the parameter ranging from 1.8 to 1.96 to take into account non perfect signal inversion). The ^{1}H chemical shifts were externally referenced to water at 4.8 ppm (relative to TMS, tetramethyl silane) as a secondary reference, and are given with an accuracy of 0.4 ppm. Careful temperature calibration of the probe was performed using the ^{207}Pb resonance of $Pb(NO_3)_3$,[5] the ^{119}Sn resonance of $Pr_2Sn_2O_7$ above 400 °C,[6] and/or the ^{79}Br signal of KBr. The sample temperatures quoted subsequently have all been corrected, and have an accuracy of ± 10 °C. NMR data were processed with MatLab and MatNMR.[7]

Random Walk Model

Proton jump frequencies are calculated from the proton diffusivity and the ambipolar diffusivity between proton and deuterium, assuming a 3D random walk[8], $\omega = D_H \gamma^{-1} a^{-2}$ (γ is a geometric factor and a is the jump distance). The geometric factor and averaged jump distance for the octahedral oxygen sites in perovskite are taken to be 8/6 and $a_0 / \sqrt{2}$, respectively, where a_0 is the measured lattice parameter, 4.2295 Å.

DOI: 10.1038/NMAT3638

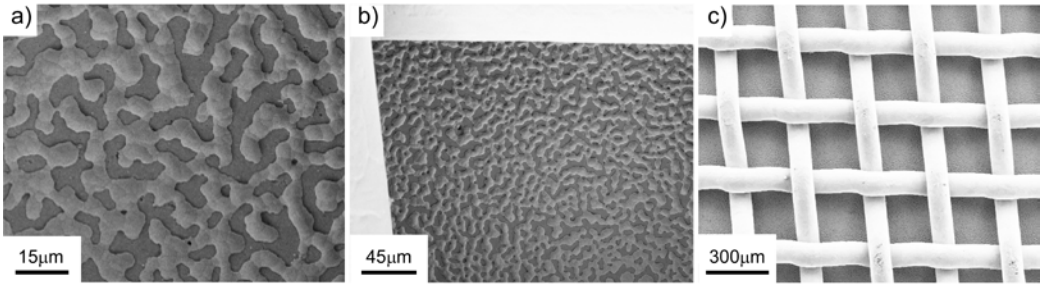

Figure S1. SEM images of an interconnected porous silver electrode (light grey) deposited on a 20 at% yttrium-doped barium zirconate (BYZ20) pellet (dark grey) at various magnifications. The white grid evident in b) and c) is a silver current collector attached on the silver electrode.

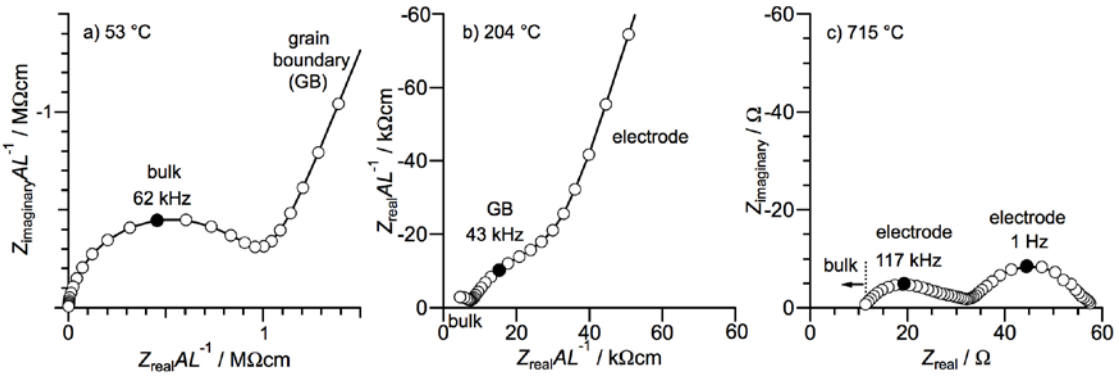

Figure S2. Nyquist representations of AC impedance spectra collected from BYZ20 at a) 53 °C, b) 204 °C and c) 715 °C. The former two were measured under a regular water partial pressure of 0.023 atm, whereas the latter was under heavy water partial pressure of 0.028 atm, just prior to the initiation of D_2O-H_2O exchange measurements (Fig. S5). The impedance response corresponding to bulk, grain boundary (GB), and electrode behavior are noted in each plot. At 715 °C, the grain boundary contribution to the electrolyte conductivity is negligible due to the large activation energy of the former.

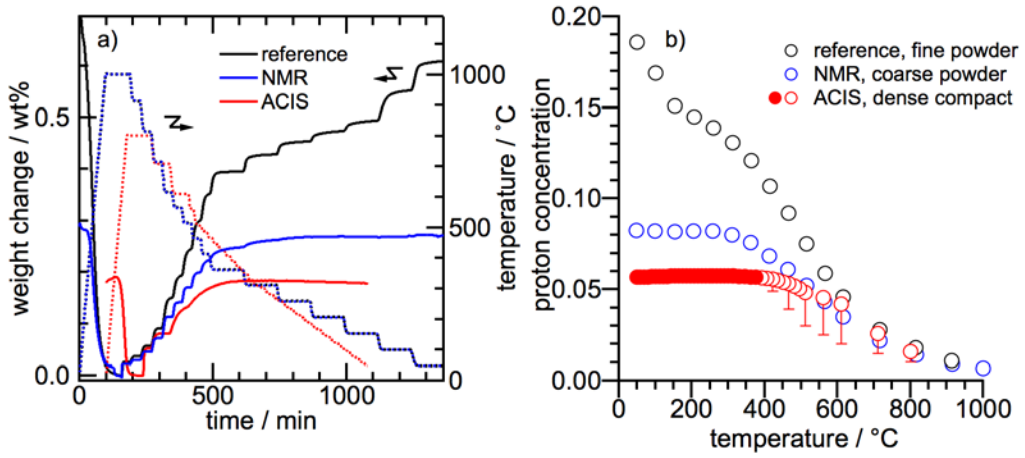

Figure S3. Hydration behavior of BYZ20 pellet (red) and coarse powder (blue) samples, presented in comparison to that of attrition-milled fine powder (black). Closed red circles represent the proton concentration utilized in obtaining the proton diffusivities, Eq. (1). Bars represent uncertainties in proton concentration due to possible oxidation[2]. Identical pellets covered with porous silver electrodes on both surfaces were used in thermogravimetry and AC impedance spectroscopy. Hydration conditions for thermogravimetry and AC impedance were also identical (water partial pressure of 0.023 atm and oxygen partial pressure of 10^{-5} atm). Constant proton concentration was observed in the BYZ20 pellet below ~400 °C and in the NMR powder below ~300 °C.

DOI: 10.1038/NMAT3638

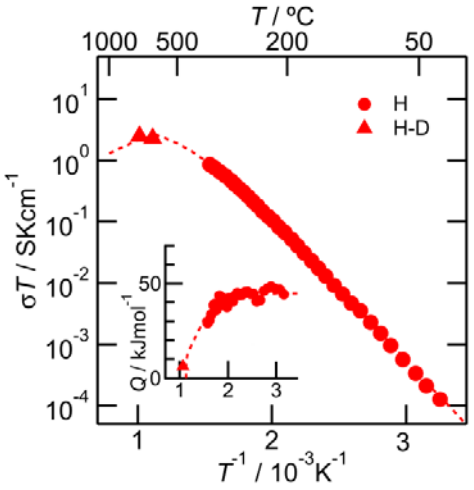

Figure S4. Arrhenius plot of the proton conductivity of BYZ20. Circles represent directly measured conductivity values. Triangles represent conductivity values computed from the ambipolar diffusivity (H_2O-D_2O exchange experiments) and the proton concentration (TGA measurements). Inset shows the apparent activation energy.

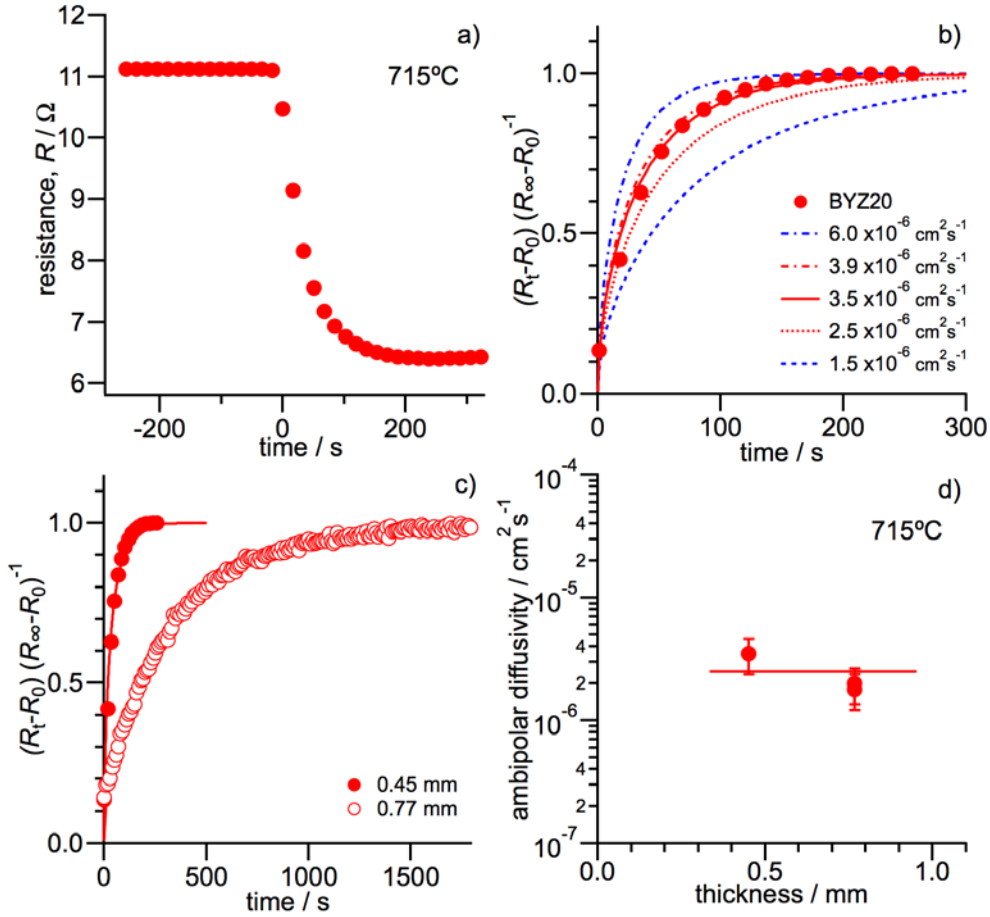

Figure S5. Example of D_2O-H_2O exchange data for direct determination of the ambipolar diffusion coefficient between proton and deuterium, $\tilde{D}_{H-D}$, in BYZ20 at 715 °C using a sample 0.45 mm in thickness: a) raw and b) normalized resistance values obtained upon a change in atmosphere from $pD_2O \sim 0.028$ atm[4] to $pH_2O = 0.027$ atm. The relaxation behavior was analyzed in the non-steady state solution of the Fick's second law for one-dimensional diffusion into a plane sheet (of thickness $2l$)[9],

$$\frac{C(x,t)-C_0}{C_1-C_0} = 1-\frac{4}{\pi}\sum_{n=0}^{\infty}\frac{(-1)^n}{2n+1}\exp\left(\frac{-\tilde{D}(2n+1)^2\pi^2 t}{4l^2}\right)\frac{\cos(2n+1)\pi x}{2l} \qquad \text{(S1)}$$

where $C(x,t)$ is the proton concentration at position, x, and time, t, C_0 and C_1 are the initial and final proton concentration, respectively, and n is the set of positive integers. The solution is expressed with respect to normalized resistance as[3]

$$\frac{R(t)-R(0)}{R(\infty)-R(0)} = \frac{1}{2l}\int_{-l}^{l}\frac{1}{\left(1-\frac{R(\infty)}{R(0)}\right)+\frac{R(\infty)}{R(0)}\frac{C_1}{C(x,t)}}dx \qquad \text{(S2)}$$

where $R(t)$, $R(0)$ and $R(\infty)$ are, respectively, the total resistance of the sample at time, t, zero, and infinity. The value of $\tilde{D}_{H-D}$ was extracted using an interactive computational procedure, in which an initial guess of $\tilde{D}_{H-D}$ was used to compute a proton concentration

DOI: 10.1038/NMAT3638

profile at time t according to eq. (S1). From the concentration profile, the resistance relaxation was then computed according to eq. (S2). The computed normalized resistance curves for several candidate values of ambipolar diffusivity are shown as lines in b, with the solid red line corresponding to the best fit. These expressions are valid when diffusion in the bulk, as opposed to reaction on the surface, is rate-limiting. Measurements of samples of differing thicknesses (0.45 mm and 0.77 mm in c and d) yielded almost identical values of $\tilde{D}_{H-D}$, confirming diffusion-limited kinetics in solid. The analysis approach also ignores the slight change in diffusivity over the course of the relaxation process. The maximum error due to the assumption of constant diffusivity is estimated at 32%.

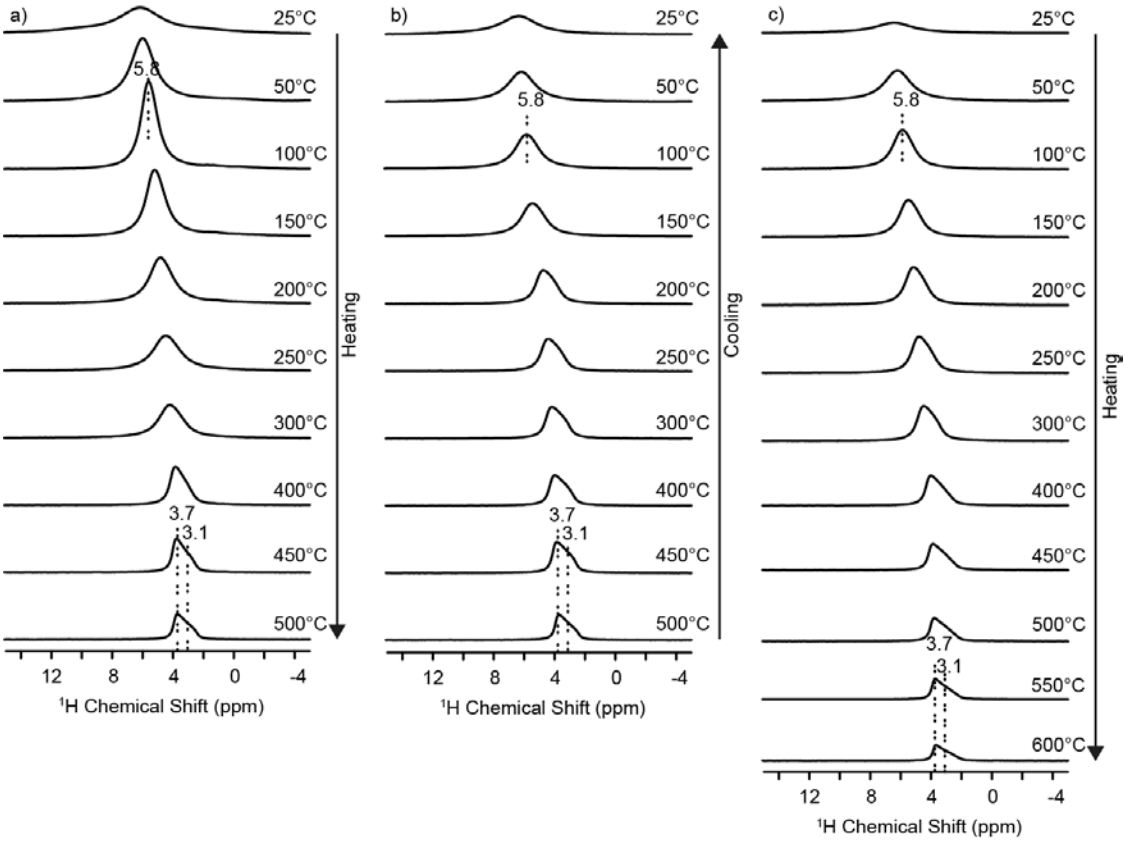

Figure S6. High temperature ^{1}H MAS NMR experiments obtained during three successive temperature runs at 360 MHz: a) first heating up to 500 °C, b) first cooling down to room temperature, and c) second heating up to 600 °C. A shoulder peak emerges at 200 °C on the lower frequency side of the main peak. The intensity of each spectrum reflects the proton concentration after Boltzmann factor correction. The low spectral intensities observed at 25 and 50 °C are a result of the slower magic angle spinning rate (4 kHz), compared with those at higher temperatures (6 kHz). Experiments were performed by using a Doty probe on a 360 MHz Chemagnetics Infinity system. The frequency separation between the two peaks places an upper bound on the time scale of proton exchange between these environments. Specifically, coalescence requires an exchange frequency greater than $2^{-1/2}\pi\Delta\nu$,[10] implying, for the observed 0.6 ppm difference in peak positions ($\Delta\nu$) (at a ^{1}H Larmor frequency of 360 MHz), that exchange between the two sites can occur at a rate no greater than 0.5 kHz.

DOI: 10.1038/NMAT3638

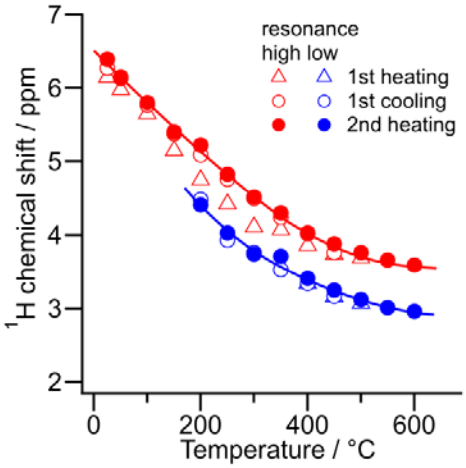

Figure S7. ^{1}H chemical shifts for the two proton environments (measured at 360 MHz). Chemical shift of the high frequency resonance, observed at all temperatures, is shown as red symbols, whereas that of the low frequency resonance, resolved at 200 °C and above, is shown as blue symbols. Uncertainty in the peak values is smaller than the symbol sizes. The chemical shift for both resonances decreases with increasing temperature, approaching, at 600 °C, 3.6 and 3.0 ppm, respectively for the high and low frequency resonances.

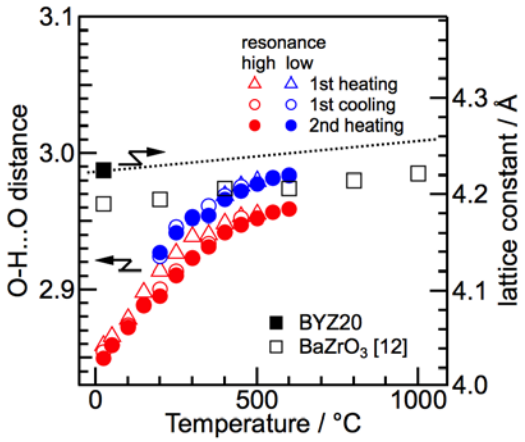

Figure S8. A comparison of oxygen-oxygen distances in barium zirconates as implied by the ^{1}H chemical shift and as determined from the crystal structure. The former is evaluated using a reported empirical relationship between ^{1}H chemical shift and oxygen-oxygen distance in the O-H…O hydrogen bond[11]. The latter, an average of all the O-O octahedral edge distances, is the result from simply taking the lattice constant and multiplying by $\sqrt{2}/2$. Data for undoped $BaZrO_3$, for which the thermal expansion behavior has been reported,[12] is shown in addition to the room temperature data for BYZ20 (this work). At room temperature, the O-H…O distance is apparently much smaller than the averaged O-O distance in both BYZ20 and undoped $BaZrO_3$. It is not surprising that the occurrence of hydrogen bonds would bring oxygen atoms closer together than in the average structure. One also observes that the apparent O-H…O distance for the high frequency resonance is, by definition, smaller than that of the low frequency resonance. Within the context of our trapped proton model, this implies that the octahedral edge distance in YO_6 is more severely shortened upon hydrogen bond formation than is the O-O distance of the ZrO_6 octahedron, despite the larger ionic radius of Y^{3+} than Zr^{4+}. In addition, the O-H…O distance for both trapped and trap-free protons increases with increasing temperature. The increase is greater than what would be predicted based on the thermal expansion behavior alone. It implies that the hydrogen bond, the strength of which is reflected in the proximity of the donor and acceptor oxygen atoms, has weakened at high temperatures. At 500 °C and above, at which dehydration becomes significant, the O-H…O distance approaches the value of the O-O distances of dehydrated BYZ20 and $BaZrO_3$.

DOI: 10.1038/NMAT3638

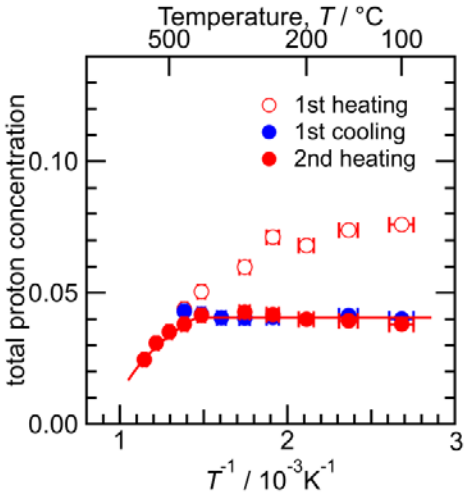

Figure S9. Total proton concentration in BYZ20 NMR powder as a function of temperature. The initial proton concentration measured by thermogravimetry, ~0.08 below 250 °C under $p\mathrm{H_2O}$ = 0.023 atm (Figure S3), was utilized for the ^{1}H NMR spectra-proton concentration conversion. A Boltzmann factor correction of $\hbar\gamma_0 B_0 / (2k_B T)$ was applied to correct for the variation in spin-state population as a function of temperature, where $\hbar$ is the reduced Planck constant, γ_0 is the gyromagnetic ratio, and B_0 is the applied magnetic field. On the first heating, the sample dehydrates above 150 °C and the proton content decreases to ~0.04 at 500 °C. On the subsequent cooling and second heating, the proton concentration is almost constant within this temperature window, indicating that no further dehydration occurs and demonstrating the reproducibility of the results.

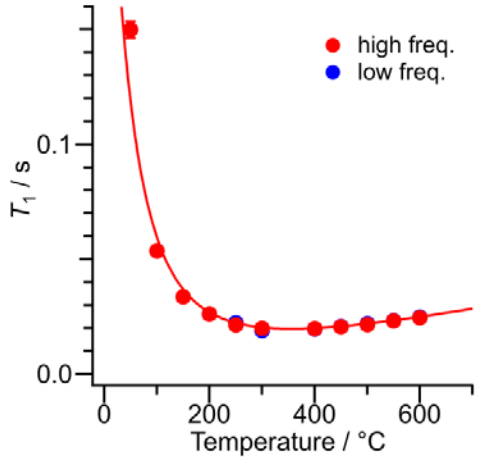

Figure S10. 360 MHz ^{1}H Spin lattice relaxation time, T_1, plotted against temperature. Error bars determined at 95 % confidence are within the symbols. T_1 values obtained for the low frequency response (trap-free site) are almost identical to those of the high frequency response (trap site), and a T_1 minimum of 20 ms is observed for both sites at 400 °C. The upper limit for exchange between the two sites is 0.5 kHz (based on the criterion for coalescence, Fig. S6). Slow exchange between the trapped and non-trapped sites, occuring at a rate that is significantly faster than T_1 ($1/T_1 = 0.05$ kHz) can plausibly explain the similar relaxation behavior of the two sites. In addition, migration of mobile protons, even in the absence of site exchange, can establish the T_1 relaxation behavior in trapped sites, and is another plausible explanation for the similar T_1 values.

DOI: 10.1038/NMAT3638

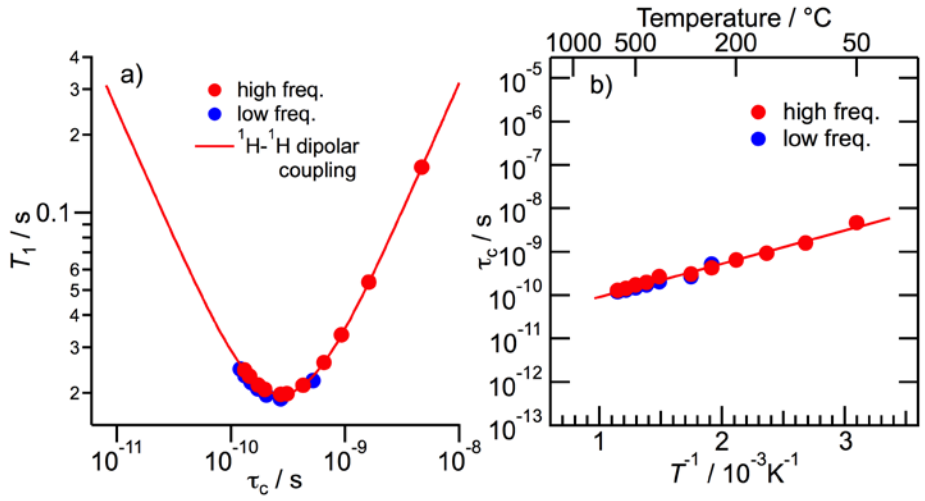

Figure S11. a) Plot of spin-lattice relaxation time, T_1, against correlation time, τ_C, for proton motion and b) τ_C plotted in Arrhenius plot. The correlation time was obtained by using

$$\frac{1}{T_1} = \frac{3}{10}\frac{\gamma_H^4 \hbar^2}{\sum_j r_{ij}^6}\left[\frac{\tau_C}{1+\omega^2\tau_C^2} + \frac{4\tau_C}{1+4\omega^2\tau_C^2}\right] \quad \text{(S3)}$$

assuming isotropic motion and a relaxation mechanism dominated by ^{1}H - ^{1}H dipolar couplings[13]. Here, γ_H, r_{ij}, ω and τ_c are the gyromagnetic ratio of the proton spin I, the distance between spins, the Larmor frequency, and the correlation time of the proton motion, respectively. T_1 shows minimum at 400 °C. The activation energies for the high and low frequency responses are -13±1 and -14±2 kJmol^{-1}, respectively.

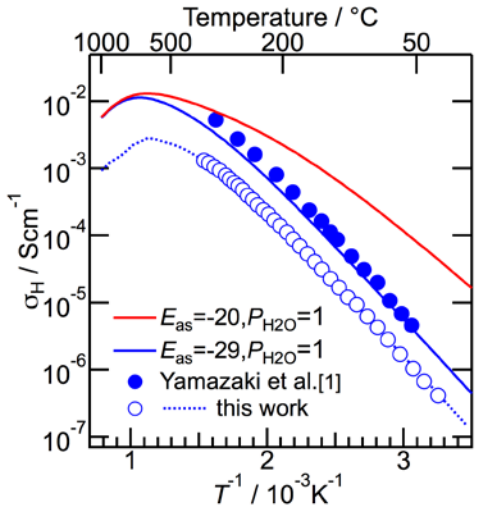

Figure S12. Measured and predicted values of proton conductivity for doped barium zirconates. Measured values (circles) are from the present work (open) and a previous study of BYZ20[1] (solid). The solid lines are predictions computed using the proton diffusivity of eq. (3) and maximum proton concentrations derived from the equilibrium hydration behavior of BYZ20[14] taking pH$_2$O = 1 atm. The calculated curves correspond to proton-dopant association energies of -20 and -29 kJ/mol (red and blue solid lines, respectively). Identifying a dopant that possesses binding energy, E_{as}, of -20 kJ/mol (as has been theoretically suggested for Gd-doping[15]) would enhance proton conductivity by a factor of ~2 at 350 °C.

DOI: 10.1038/NMAT3638

Information S13. Proton-dopant association and proton transport in proton-conducting oxides

The analysis of proton transport under the influence of proton-dopant association is described here. First, the defect chemistry of proton-dopant association is defined in S13-1 (making use of Kröger-Vink notation), which is then correlated to the macroscopic proton transport in S13-2. Analytical procedures for obtaining the proton diffusion parameters and the thermodynamic association parameters are described in S13-3.

S13-1. Defect chemistry of proton-dopant association

Yttrium doping on the zirconium site of barium zirconate is carried out with the objective of creating oxygen vacancies of effectively positive charge, $V_O^{\bullet\bullet}$, which result to provide site and charge balance against the effectively negatively charged yttrium species, Y'_{Zr}. Upon exposure of this system to water vapor, H_2O is incorporated into the bulk such that some formerly vacant and formerly normal oxygen sites become occupied by hydroxyl species, $OH_O^{\bullet}$. The positively charged protons (equivalent to the hydroxyl groups) can be attracted to the negatively charged dopant species, creating neutral complexes. This association or proton trapping reaction is given as:

$$OH_{O.f}^{\bullet} + Y'_{Zr.f} = (OH_O^{\bullet} Y'_{Zr})^{\times} \tag{S4}$$

where $(OH_O^{\bullet} Y'_{Zr})^{\times}$ is the neutral complex formed of immobile yttrium and trapped protons, and the subscript *f* explicitly denotes the association-free species. In the ideal solution limit, the equilibrium constant of this association reaction is expressed as

$$K_{as} = \frac{[(OH_O^{\bullet} Y'_{Zr})^{\times}]}{[OH_{O.f}^{\bullet}][Y'_{Zr.f}]} = A\exp\left(-\frac{E_{as}}{RT}\right) \tag{S5}$$

where square brackets indicate concentrations, E_{as} is the association enthalpy (a negative value indicates an attractive interaction), and A is a pre-exponential term related to the association entropy.

In the presence of trapping effects, the electroneutrality condition becomes

$$[OH_{O.f}^{\bullet}] + 2[V_O^{\bullet\bullet}] + [h^{\bullet}] = [Y'_{Zr.f}] \tag{S6}$$

where the electronic hole concentration, $[h^{\bullet}]$ is included in eq. (S6) and the following for completeness[2]. However, because holes are only important at relatively high temperatures[16] (higher than those explored in the present work), these defects have little impact and are largely treated as negligible. Conservation of proton and yttrium species in the system imply, respectively,

$$[OH_O^{\bullet}]_{total} = [OH_{O.f}^{\bullet}] + [(OH_O^{\bullet} Y'_{Zr})^{\times}] \tag{S7}$$

and

$$[Y'_{Zr}]_{total} = [Y'_{Zr.f}] + [(OH^{\bullet}_{O}Y'_{Zr})^{\times}] \quad \text{(S8)}$$

The subscript, total, written outside of the bracket, explicitly expresses the total defect concentration. Combining the electroneutrality condition, eq. (S6), and the mass conservation conditions, eqs. (S7) and (S8), yields the global electroneutrality condition, irrespective of the extent of association:

$$[OH^{\bullet}_{O}]_{total} + 2[V^{\bullet\bullet}_{O}] + [h^{\bullet}] = [Y'_{Zr}]_{total} \quad \text{(S9)}$$

In a system with trapped carriers, the diffusivity is proportional to the fraction of free carriers. Here, the fraction of free protons is

$$\frac{C_{H.free}}{C_{H.total}} = \frac{[OH^{\bullet}_{O.f}]}{[OH^{\bullet}_{O.f}] + [(OH^{\bullet}_{O}Y'_{Zr})^{\times}]} = \frac{1}{1 + [(OH^{\bullet}_{O}Y'_{Zr})^{\times}]/[OH^{\bullet}_{O.f}]} \quad \text{(S10)}$$

Inserting eq. (S5) into eq. (S10) yields this fraction in terms of the proton-dopant association behavior:

$$\frac{C_{H.free}}{C_{H.total}} = \left(1 + [Y'_{Zr.f}]K_{as}\right)^{-1} \quad \text{(S11)}$$

which is alternatively expressed as

$$C_{H.free} = C_{H.total}(1 + [Y'_{Zr.f}]K_{as})^{-1} \quad \text{(S12)}$$

When $[OH^{\bullet}_{O.f}] + [h^{\bullet}] << 2[V^{\bullet\bullet}_{O}]$, $[Y'_{Zr.f}]$ is nearly equal to $2[V^{\bullet\bullet}_{O}]$, eq. (S6). Thus, the association-free proton concentration is reduced to

$$C_{H.free} = C_{H.total}(1 + 2[V^{\bullet\bullet}_{O}]K_{as})^{-1} \quad \text{(S13)}$$

The trapped proton concentration is then simply obtained from

$$[(OH^{\bullet}_{O}Y'_{Zr})^{\times}] = C_{H.total} - C_{H.free} \quad \text{(S14)}$$

Accordingly, knowledge of K_{as} (along with the independently known or measured values of $[V^{\bullet\bullet}_{O}]$ and $C_{H.total}$) implies the impact of trapping on diffusivity (through its impact on carrier concentration) is known, or, conversely, from the knowledge of diffusivity, the parameters of K_{as} can be determined.

S13-2. Proton diffusion under proton-dopant association

In the absence of defect trapping effects ionic diffusivity typically displays Arrhenius behavior, expressed here in the case of free protons as

$$D_{H.free} = D_0 \exp\left(-\frac{E_a}{RT}\right) \quad \text{(S15)}$$

where $D_{H.free}$ is the diffusivity of free protons, E_a is the activation energy for proton motion, and D_0 is a pre-exponential (constant) factor. At a low temperature, however, at which some protons are trapped at dopant sites such that they are integrated into neutral,

DOI: 10.1038/NMAT3638

immobile species, eq. (S4), the observed or apparent diffusivity is reduced relative to $D_{H.free}$ in accord with the reduced concentration of mobile charge carriers, becoming

$$D_{H.app} = D_{H.free}\frac{C_{H.free}}{C_{H.total}} \tag{S16}$$

This expression is exactly the same as that derived in the cases of hydrogen in metals[17]. Using eqs. (S5), (S11), (S15), and (S16), the apparent proton diffusivity is then expressed as

$$\begin{aligned} D_{H.app} &= D_0 \exp\left(-\frac{E_a}{RT}\right)\left[1+[Y'_{Zr.f}]K_{as}\right]^{-1} \\ &= D_0 \exp\left(-\frac{E_a}{RT}\right)\left[1+[Y'_{Zr.f}]A\exp\left(-\frac{E_{as}}{RT}\right)\right]^{-1} \end{aligned} \tag{S17}$$

the result quoted in eq. (3) of the main text.

Two temperature regimes emerge:

a) At *high temperatures*, at which the association reaction is negligible ($[Y'_{Zr.f}]K_{as} << 1$), the association-free proton fraction in eq. (S11) is unity, and (S16) simply reduces to

$$D_{H.app} = D_{H.free} = D_0 \exp\left(-\frac{E_a}{RT}\right). \tag{S18}$$

Accordingly, the apparent proton diffusivity appears linear in an Arrhenius plot and displays activation energy E_a.

b) At low temperatures, at which the association reaction is dominant ($[Y'_{Zr.f}]K_{as} >> 1$), the association-free proton concentration becomes negligible and (S11) reduces to

$$\frac{C_{H.free}}{C_{H.total}} = ([Y'_{Zr.f}]K_{as})^{-1} \tag{S19}$$

When the hole concentration is negligible, eq. (S6) is reduced to $[Y'_{Zr.f}] \approx 2[V_O^{\bullet\bullet}]$ and

$$\frac{C_{H.free}}{C_{H.total}} = (2[V_O^{\bullet\bullet}]K_{as})^{-1} \tag{S20}$$

Inserting into (S16) yields

$$D_{H,app.T_L} = D_{H.free}(2[V_O^{\bullet\bullet}]K_{as})^{-1} \tag{S21}$$

into which we insert the expressions for K_{as} and $D_{H.free}$ (eqs. (S5) and (S15)), respectively) to obtain

$$D_{H,app.T_L} = \frac{D_0}{2[V_O^{\bullet\bullet}]A}\exp\left(-\frac{E_a - E_{as}}{RT}\right) = B\exp\left(-\frac{Q}{RT}\right) \tag{S22}$$

where

$$B = \frac{D_0}{2[V_O^{\bullet\bullet}]A} \tag{S23}$$

Over a moderate temperature range or at sufficiently low temperatures, changes in the material hydration state are negligible and B (or $[V_O^{\bullet\bullet}]$) is constant. In such case, the apparent proton diffusivity, $D_{H,app.T_L}$, is linear when plotted in Arrhenius form and has an activation energy of Q (=E_a – E_{as}), eq. (S24), that is greater than E_a (where E_{as} is a negative value).

Considering the entire temperature range, we can obtain the relevant expression for the apparent diffusivity by inserting eqs. (S6), (S23), and (S24) into eq. (S17) applicable at all temperatures:

$$D_{H.app} = D_0 \exp\left(-\frac{E_a}{RT}\right)\left[1+\frac{D_0}{B}\left(1+\frac{[OH_{O.f}^{\bullet}]+[h^{\bullet}]}{2[V_O^{\bullet\bullet}]}\right)\exp\left(-\frac{E_a-Q}{RT}\right)\right]^{-1} \tag{S25}$$

This form contains four unknown constants (D_0, E_a, A and Q) and two temperature-dependent variables, ($[OH_{O.f}^{\bullet}]+[h^{\bullet}]/(2[V_O^{\bullet\bullet}])$ and B, eq. (S23)). Under the condition that $\frac{[OH_{O.f}^{\bullet}]+[h^{\bullet}]}{2[V_O^{\bullet\bullet}]}$ is much smaller than unity, the apparent proton diffusivity is reduced to

$$D_{H.app} = D_0 \exp\left(-\frac{E_a}{RT}\right)\left[1+\frac{D_0}{B}\exp\left(-\frac{E_a-Q}{RT}\right)\right]^{-1} \tag{S26}$$

and now only D_0, E_a, Q and B are unknown. It is noteworthy that although the direct impact of dehydration on the relationship between $D_{H,app}$ and conductivity was already accounted for, there is an additional role of dehydration through its influence on the equilibration between trapped and free protons, eq. (S4).

S13-3. Obtaining association energy and association-free proton diffusion parameters in proton-dopant association (trapping) model

The diffusion parameters were obtained in two steps. We first estimate the parameters under an assumption of negligible dehydration (constant B) and then account for dehydration (variable B).

Initial values for Q and B were obtained from the low-temperature linear regime in the Arrhenius plot of ln(D) vs. 1/T, eq. (S22). These constants were then inserted as fixed quantities into eq. (S26). Fitting eq. (S26) to the apparent proton diffusivities provides the values of D_0 and E_a (using Igor Pro, WaveMetrics Inc.). The value of A was also calculated in eq. (S23) by inserting the known constants B and $[V_O^{\bullet\bullet}]$ and obtained D_0.

DOI: 10.1038/NMAT3638

The diffusion parameters accounting for dehydration were recomputed. The temperature dependence of $B(=D_0/2[V_O^{\bullet\bullet}]A)$ was obtained using variable $[V_O^{\bullet\bullet}]$ calculated in eq. (S9) (negligible $[h^{\bullet}]$ assuming $[OH_{O.f}^{\bullet}]+[h^{\bullet}]<<2[V_O^{\bullet\bullet}]$) and the obtained A. Using these variable B, the diffusivities were refitted by eq. (S26) and the parameters, D_0 and E_a, accounting for dehydration, were determined. The value of E_{as} for proton-dopant association reaction is simultaneously obtained in eq. (S24) while the value of A is obtained from eq. (S23). In Table S13-1 the parameters extracting under the assumptions of fixed and temperature dependent B are presented.

Table S13-1. Associated and association-free proton concentration computed in proton-dopant association model, eq. (2).

assumption	D_0 (cm^2s^{-1})	E_a ($kJmol^{-1}$)	$[Y_{Zr}']_f$	A	E_{as} ($kJmol^{-1}$)
negligible dehydration	$(4\pm2)\times10^{-5}$	17±4	0.14	$(6\pm2)\times10^{-2}$	-28±2
dehydration	$(3\pm2)\times10^{-5}$	16±4	$D_0A^{-1}f^{-1}(T)$*	$(5\pm1)\times10^{-2}$	-29±2

* $f(T)=0.003+0.012\left[1+\exp\left(-\frac{T^{-1}-0.0011}{0.00012}\right)\right]^{-1}$

Information S14. Validation of assumption in obtaining diffusion parameters in proton-dopant association model

To obtain the diffusion parameters in the proton-dopant association model, we assumed $[OH_{O.f}^{\bullet}]+[h^{\bullet}]/(2[V_O^{\bullet\bullet}])<<1$. The validity of this assumption is evaluated and confirmed here. The term $([OH_{O.f}^{\bullet}]+[h^{\bullet}])/(2[V_O^{\bullet\bullet}])$ is expressed from eqs. (S6), (S8), and (S9) as

$$\frac{[OH_{O.f}^{\bullet}]+[h^{\bullet}]}{2[V_O^{\bullet\bullet}]}=\frac{[Y_{Zr}']_{total}-[(OH_O^{\bullet}Y_{Zr}')^X]}{[Y_{Zr}']_{total}-([OH_O^{\bullet}]_{total}+[h^{\bullet}])}-1 \qquad \text{(S27)}$$

On the right hand side of this equation, all defect concentrations are known except $[h^{\bullet}]$. At low temperatures, the hole concentration is negligible in absolute terms.[16] At high temperatures, although oxidation of the oxide may lead to non-zero hole concentration, we conclude, based on prior studies, that $[OH_O^{\bullet}]_{total}+[h^{\bullet}]$ will exceed $[OH_O^{\bullet}]_{total}$ by no more than 6% under our experimental conditions[2]. Thus, eq. S(27) becomes

$$\frac{[OH_{O.f}^{\bullet}]+[h^{\bullet}]}{2[V_O^{\bullet\bullet}]}\approx\frac{[Y_{Zr}']_{total}-[(OH_O^{\bullet}Y_{Zr}')^X]}{[Y_{Zr}']_{total}-[OH_O^{\bullet}]_{total}}-1 \qquad \text{(S28)}$$

which can be easily calculated. As shown in Fig. S14, the so-computed value of $[OH_{O.f}^{\bullet}]+[h^{\bullet}]/(2[V_O^{\bullet\bullet}])$ is much smaller than unity over the entire temperature range of interest, with a peak value of only 0.2 occurring at around ~500 °C.

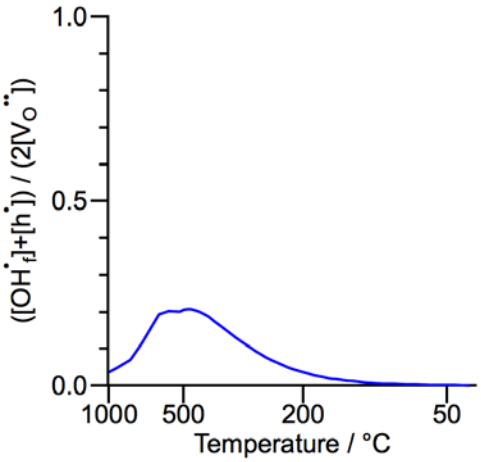

Figure S14. Validation of assumption in proton-dopant association model: $([OH_{O.f}^{\bullet}]+[h^{\bullet}])/(2[V_O^{\bullet\bullet}]) << 1$.

References

1 Yamazaki, Y., Hernandez-Sanchez, R. & Haile, S. M. High total proton conductivity in large-grained yttrium-doped barium zirconate. *Chemistry of Materials* **21**, 2755-2762 (2009).

2 Yamazaki, Y., Yang, C. K. & Haile, S. M. Unraveling the defect chemistry and proton uptake of yttrium-doped barium zirconate. *Scripta Materialia* **65**, 102-107 (2011).

3 Okuyama, Y., Kurita, N. & Fukatsu, N. Incorporation of hydrogen in barium-doped alpha-alumina. *Solid State Ionics* **180**, 175-182 (2009).

4 Lide, D. R. *CRC Handbook of Chemistry and Physics, Internet Version*. Internet Version edn, (CRC Press, 2005).

5 Bielecki, A. & Burum, D. P. Temperature-Dependence of Pb-207 Mas Spectra of Solid Lead Nitrate - an Accurate, Sensitive Thermometer for Variable-Temperature Mas. *Journal of Magnetic Resonance Series A* **116**, 215-220 (1995).

6 Vanmoorsel, G. J. M. P., Vaneck, E. R. H. & Grey, C. P. $Pr_2Sn_2O_7$ and $Sm_2Sn_2O_7$ as High-Temperature Shift Thermometers in Variable-Temperature Sn-119 MAS NMR. *Journal of Magnetic Resonance Series A* **113**, 159-163 (1995).

7 van Beek, J. D. MatNMR: A flexible toolbox for processing, analyzing and visualizing magnetic resonance data in MatLab((R)). *Journal of Magnetic Resonance* **187**, 19-26 (2007).

8 Shewmon, P. *Diffusion in solids*. 2nd edn, (TMS, 1989).

9 Crank, J. *The mathematics of diffusion*. 2nd edn, (Clarendon Press, 1975).

DOI: 10.1038/NMAT3638

10 Levitt, M. H. *Spin dynamics*. (John Wiley & Sons, Ltd, 2000).

11 Eckert, H., Yesinowski, J. P., Silver, L. A. & Stolper, E. M. Water in Silicate-Glasses - Quantitation and Structural Studies by ^{1}H Solid Echo and MAS-NMR Methods. *Journal of Physical Chemistry* **92**, 2055-2064 (1988).

12 Zhao, Y. H. & Weidner, D. J. Thermal Expansion of $SrZrO_3$ and $BaZrO_3$ Perovskites. *Phys Chem Miner* **18**, 294-301 (1991).

13 Steigel, A. & Spiess, H. W. *Dynamic NMR Spectroscopy*. (Springer-Verlag, 1978).

14 Yamazaki, Y., Babilo, P. & Haile, S. M. Defect Chemistry of Yttrium-Doped Barium Zirconate: A Thermodynamic Analysis of Water Uptake. *Chemistry of Materials* **20**, 6352-6357 (2008).

15 Stokes, S. J. & Islam, M. S. Defect chemistry and proton-dopant association in $BaZrO_3$ and $BaPrO_3$. *Journal of Materials Chemistry* **20**, 6258-6264, (2010).

16 Nomura, K. & Kageyama, H. Transport properties of $Ba(Zr_{0.8}Y_{0.2})O_{3-\delta}$ perovskite. *Solid State Ionics* **178**, 661-665 (2007).

17 Oriani, R. A. The diffusion and trapping of hydrogen in steel. *Acta Metallurgica* **18**, 147-157 (1970).